Received 4 June 2024; accepted 27 July 2024. Date of publication 2 August 2024; date of current version 22 November 2024.

Digital Object Identifier 10.1109/OJAP.2024.3437687

3-D Chipless RFID Tag for Anti-Counterfeiting Applications

SUVADEEP CHOUDHURY [1,2] (Senior Member, IEEE), FILIPPO COSTA [1] (Senior Member, IEEE), GIULIANO MANARA [1] (Life Fellow, IEEE), AND SIMONE GENOVESI [1] (Senior Member, IEEE)

[1]Dipartimento di Ingegneria dell'Informazione, University of Pisa, 56122 Pisa, Italy
[2]Department of Electronics and Communication Engineering, The LNM Institute of Information Technology, Jaipur 302031, India

CORRESPONDING AUTHOR: S. CHOUDHURY (e-mail: suvadeep.choudhury.in@ieee.org)

This work was supported by the Italian Ministry of Education and Research (MUR) in the framework of the Crosslab and Forelab Projects (Departments of Excellence).

ABSTRACT A novel methodology for designing Chipless Radio Frequency Identification (RFID) tags realized using the Additive Manufacturing technologies and exhibiting a high number of identification states is proposed and investigated. An encoding scheme based on the resonances and anti-resonances of the input impedance of the resonator is employed for identifying the tag, which is achieved by exploiting the set of zero-crossing points of the tag reactance. A tolerance analysis is also performed to avoid any ambiguity in the reading process and to minimize the redundancy, thus providing unique electromagnetic signatures which are also suitable for anti-counterfeiting applications. Several prototypes have been fabricated and tested to assess the practical implementation of the proposed encoding scheme.

INDEX TERMS Additive manufacturing, chipless RFID, dielectric resonator, radio frequency identification (RFID), square cavity.

I. INTRODUCTION

THE PRODUCT counterfeiting is a major concern in today's scenario, being a severe threat for several businesses, including electronics, pharmaceuticals, luxury items, and consumer goods [1]. Such counterfeited products result in heavy economical losses, posing serious risk to public health and safety, and result in vulnerabilities in the supply chain management, ultimately resulting in the reputation and loss of trust in legitimate brands and products [2], [3]. From a hardware perspective, this problem can be tackled by embedding into the device or the object of interest, a unique and observable characteristic which is able to provide an identifiable information often referred to as *fingerprinting* [4]. This identification approach is based on a physical-layer device tagging and can be applied to both active and passive items. In the former case, the fingerprint is obtained by exploiting the effects on the generated RF signal by manufacturing tolerances or components imperfections of the analog circuitry [5], [6], [7], [8]. A passive item requires an added physical feature to realize the fingerprint such as holograms [9], [10], [11], ultraviolet images or hidden text in a document [12]. Radio Frequency Identification (RFID) represents a subset of these added authentication characteristics, and the design approach relying on chip-based RFID structures has been recently complemented by chipless RFID ones [13], which do not require any integrated circuit.

Initially, the form factor of these chipless tags was limited to thin planar structures, which were essentially bidimensional (2D) passive devices comprising dielectric layers and conductive traces [14], [15]. In most of the proposed solutions, the fingerprint is stored in the electromagnetic field scattered by the chipless RFID tags when they are illuminated by a plane wave. The utilization of physical-layer tag signal features has emerged as a prominent approach for authentication within anti-counterfeiting solutions. This methodology frequently entails the direct extraction of physical characteristics from the signal, including the reflection coefficient [16] and measured distance [17]. Different encoding scheme have then been proposed by exploiting the amplitude [16], [18], phase [19], [20], or polarization state of the reflected field within the employed frequency bandwidth [21], [22], or using near-field readers in the time domain [23]. In this regard, the frequency domain analysis

of tags have been more popular [24], and would be the focus for the current work as well. The interrogation of chipless RFID tags is generally carried out with antennas placed both in the far as well as the near field but may require also antennas embedded directly at the tag side [18].

From the chipless RFID perspective, there has been a significant effort to incorporate hardware-based authentication methods primarily based on the natural randomness of the tag by using features of inkjet printing process [25], or the bistatic backscattering pattern [26], to name a few. Although these solutions offer a robust authentication, they place some constraints on the end user system, which has to be almost identical to the measurement setup employed to characterize the tag. A possible alternative solution that takes advantage of additive manufacturing processes has been proposed in [27] where the information is stored in the electromagnetic signature of an *electromagnetically open* 3D tag, which is controlled by realizing properly designed inclusions in it. It investigates the dependence of control over a limited number of resonances (no more than 4) on the impedance variation of a top-loaded monopole antenna embedded within an inhomogeneous dielectric medium.

The reading process involves the collection of the reflection coefficient of the tag through the use of a small RF connector. The 3D chipless tag can be implemented with different form factors in a single piece without any post-processing or gluing of two or more different parts, which is unfeasible with other fabrication processes. Moreover, it is not possible to infer the properties of the inclusions from the outside, therefore the information is concealed and any fraudulent attempt to retrieve the inner configuration would imply the destruction of the tag. The printing process can even be associated with a direct integration of the 3D chipless tag within the package.

The current work exploits a different structure, namely an *electromagnetically closed* resonator, that is able to address the lack of sufficient identification (ID) states and the cumbersome form factor that affected the aforementioned solution with the employment of suitable and cheap materials and by tailoring the number and shape of void inclusions. With the current design approach, the number of resonances is increased up to a level non reachable with the previous approach [27], although PLA has been employed in both of them. These air-filled pockets allow to realize unique fingerprints that can be associated to the target item. The encoding is obtained by exploiting the resonances and anti-resonances of the imaginary part of the measured input impedance of the tag. A tolerance analysis is also performed to minimize the risk of ID ambiguity. All these improvements are done in view of providing a fingerprint as a physical link with the object that can be then jointly integrated with the blockchain technology [28] to prevent or detect fraudulent copies. In this sense, the focus is more on avoiding any ambiguity in the fingerprint recognition and offering the robustness in its recovering without imposing severe constraints in the reader setup. A set of 3D tags is finally fabricated and tested to assess the reliability of the proposed approach toward an additional physical-layer level for anti-counterfeiting.

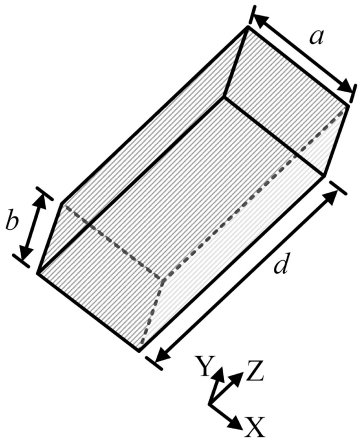

FIGURE 1. Dielectric filled square cavity resonator (metallic walls have been shown shaded).

A chipless 3D tag offers several distinctive features due to its design characteristics. Firstly, it acts as an additional layer of authentication for asset management. The tag is physically attached/ integrated/ embedded directly into the product. The detector unit, consisting of a portable Vector Network Analyzer (VNA) and a probe with an SMA connector, reads the tag by physically probing it (plug-and-play). The detector then records and validates the tag's response. Additionally, the design can be scaled up or down based on user requirements to meet the specifications of the detector. The current design serves as a proof-of-concept, demonstrating the feasibility of unambiguous coding through additive manufacturing technology.

This paper is organized as follows: Section II discusses the design conjecture with the modal characteristics, fullwave results, and the field analysis. Section III examines the encoding strategy, with the tolerance analysis for efficient non-overlapping tag retrieval. The fabrication results for PREPERM and PLA have been showcased in Section IV with successful integration within a system, and Section V providing the concluding remarks.

II. TAG DESIGN AND CHARACTERIZATION

In order to encode information, it is considered a dielectric filled rectangular metallic cavity. The starting geometry (serving as the basic design) is the structure shown in Fig. 1, hereon referred to as the one with *Solid Infill* (SI), which is a monolithic block of homogeneous material. To establish the permitivity of the material, a thin sheet of SI material is characterized using the waveguide measurement method, with a calibrated VNA in the C-band [29], [30]. The cavity operates in the TE_{10} dominant mode (given the feed location is in the xy-plane - Fig. 1), with considerable separation between this mode and its second higher order harmonic, whereas a square cavity resonator would have several

TABLE 1. Normalized electric field distribution at resonant frequencies of the Cavity(Th.: Theoretical, Em.: Eigenmode, FW: Fullwave).

Mode	Modal Electric Field	Resonant Frequency (GHz)		
		Th.	Em.	FW
TM_{110}	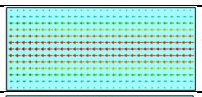	4.47	4.48	4.49
TM_{111}	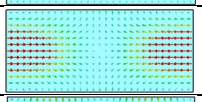	4.67	4.67	4.73
TM_{112}	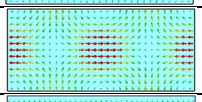	5.25	5.24	5.26
TM_{113}	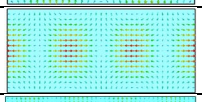	6.08	6.08	6.07
TM_{114}	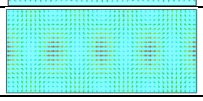	7.08	7.08	7.07

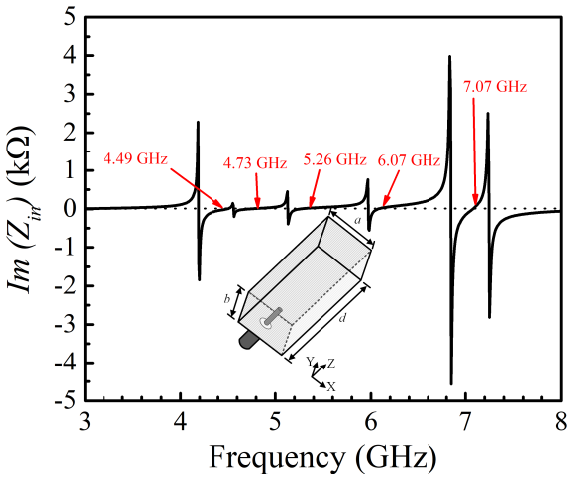

FIGURE 2. Imaginary Z_{in} for the square cavity resonator with a coaxial feed as shown in the inset.

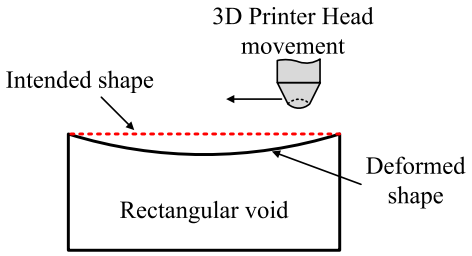

FIGURE 3. Issues with printing a rectangular void - with 90° angles.

degenerate narrowband resonances. The current application demands the need for narrowband resonances within the observed frequency bandwidth, which is considered within 3 - 10 GHz, largely adopted in chipless RFID systems. The anti-counterfeiting applications requires the tags to be unique in their characteristics while being unidentifiable for its external physical appearance. To generate such unique tags, the structure must be modified internally, while maintaining its external physical attributes. With the additive manufacturing process, air-voids can be incorporated inside the structure, which can be varied in terms of its physical dimensions and location to obtain unique tags.

A. MODAL ANALYSIS

An eigenmode analysis of the SI structure of Fig. 1 helps in identifying its natural resonances for an optimal feed placement. The structure has been analyzed for finding its symmetric resonant modes for a $= b =$ 15 mm, and $d =$ 34.5 mm, which are considered suitable dimensions for being embedded in a medium-size object. For a dielectric filled cavity, the resonant frequency of a particular mode TE_{mnp} or TM_{mnp} can be calculated from its dispersion relation as [31]:

$$f_{mnp} = \frac{c}{2\sqrt{\varepsilon_r}}\sqrt{\left(\frac{m}{a}\right)^2 + \left(\frac{n}{b}\right)^2 + \left(\frac{p}{d}\right)^2} \quad (1)$$

with m, n, p and a, b, d being the wave numbers and wall dimensions, respectively. The PREPERM®ABS1000 having $\epsilon_r = 10$ and $\tan\delta = 0.003$ at 2.4 GHz has been considered as dielectric filling. The comparison with the results of an eigenmode analysis shows a good match between them (Table 1).

B. FULL-WAVE ANALYSIS

To excite these modes, the resonant cavity structure is excited by a coaxial feeder whose inner conductor is inserted at the center of the square face and parallel to the z-axis, with the outer one grounded. The structure resonates in agreement with the theoretical and eigenmode analysis (Table 1), as it can be observed from the Zero Crossing Points (ZCP) of the imaginary part of the input impedance (e.g., $Im(Z_{in})$, reported in Fig. 2.

To increase the number of ZCPs, air voids are included within the resonator that can be then tuned to change resonance/antiresonance values. Incorporation of a rectangular void seems the primary choice for such designs, but to fabricate it, the top layer needs to be over-hanged. This results in relative bending of the over-hanged layer (as the material deposited is still in semi-solid form) resulting in changed void dimensions (Fig. 3). Additionally, as it is an air-filled void, supports are not permitted in the fabrication. Both sphere and cone have gradual increasing/ decreasing volume (unlike the rectangular void with sharp 90°), and hence can effectively be fabricated with the 3D printing technology. Hence, these two basic geometries have been considered, which will be called the *Spherical void* and the *Conical void*, respectively. The voids are preliminary placed in correspondence to the modal field maxima to provide a significant variation of the resonance/antiresonance values. The shapes subset can be clearly extended to any geometry with theoretically infinite configurations, but this work exploited only these two void types for the ease

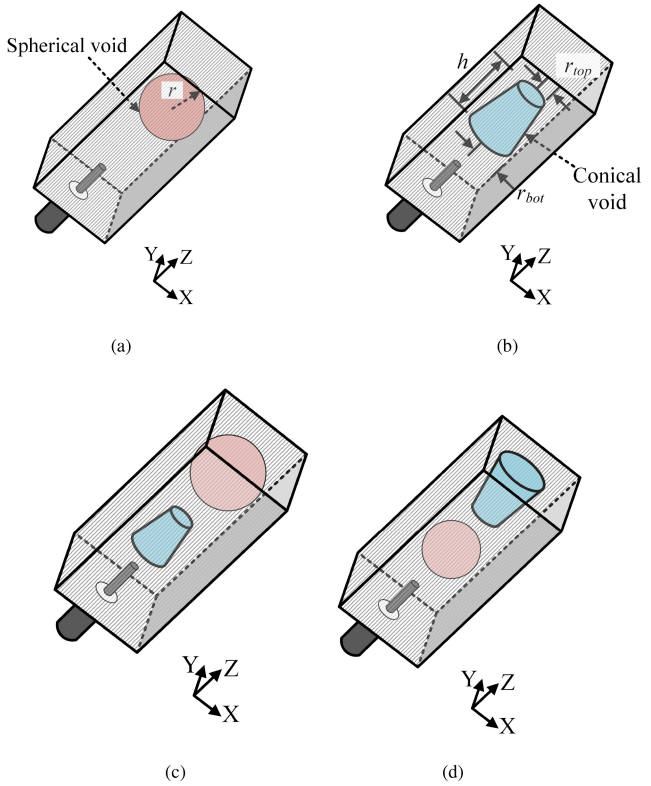

FIGURE 4. Square cavity with (a) Spherical void, (b) Conical void, and (c), (d) Combinations of the spherical and conical voids in different configurations.

of fabrication. Different combinations of these two void inclusions can be considered as described hereafter.

Spherical void only: A spherical void is placed inside the resonator (Fig. 4(a)), and the following variations are considered:

- Varying the location of the sphere center while keeping the radius (r) fixed;
- Varying both the radius (r) and center locations.

Conical void only: A conical void represented in Fig. 4(b) offers more degrees of freedom and therefore the variations are:

- Varying the location of the conical void keeping the other dimensions fixed (i.e., location variation);
- Varying the bottom radius (r_{bot}) keeping the top radius (r_{top}) constant with z-axis variation of the conical void;
- Changing the top radius (r_{top}) keeping the bottom radius (r_{bot}) constant with z-axis variation of the conical void;
- Varying r_{top}, r_{bot}, and h.

Conical and spherical void together: Two set of combinations, shown in Figs. 4(c) and 4(d) have been performed, with the following variations:

- Cone height (h) variation;
- Cone bottom radius (r_{bot}) variation;
- Cone top radius (r_{top}) variation;
- Sphere radius (r) variation;
- Spatial variations of cone and sphere locations.

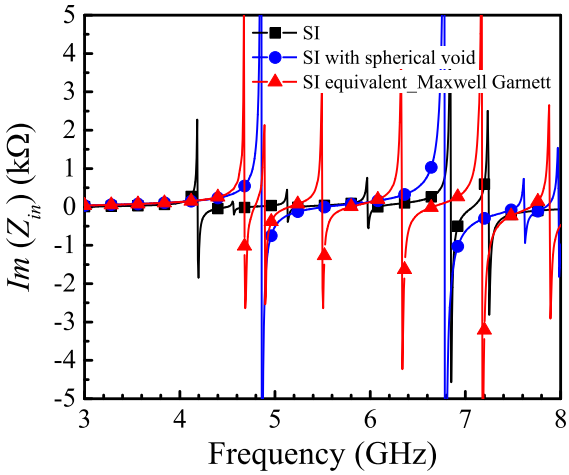

FIGURE 5. Imaginary Z_{in} of the SI structure, SI with spherical void, and its Maxwell Garnett equivalent.

These combinations of the voids have been done with the aim to generate signatures from the tags, which would serve as an identifier, to be discussed subsequently.

C. ANALYSIS OF THE FIELDS

A resonator fully filled with an equivalent dielectric material has been considered to prove that the control of the resonant frequencies is due to the tailoring of the voids, i.e., the frequency response. The value of the equivalent permittivity of this medium is calculated by resorting to the *homogenization theory* introduced by Garnett [32], [33] that exploits the permittivity values and volume fractions of the two involved materials. For a spherical void inclusion into a SI resonator, its equivalent Maxwell Garnett counterpart, can be calculated as:

$$\frac{\varepsilon_e - \varepsilon_b}{\varepsilon_e + 2\varepsilon_b} = \delta_v \frac{\varepsilon_v - \varepsilon_b}{\varepsilon_v + 2\varepsilon_b} \tag{2}$$

where, ϵ_e is the effective dielectric constant of the Maxwell Garnett equivalent, ϵ_b is the dielectric constant of the actual SI resonator, ϵ_v the dielectric constant of the void (in this case 1), and δ_v is the volume fraction of the void with respect to the SI geometry. A SI tag is then realized with the ϵ_e value obtained from (2) and the corresponding *Im (Z_{in})* is retrieved (Fig. 5). It is apparent that the resonances of this homogeneous structure are very different from those associated to the actual spherical void inclusion, as also highlighted by the internal E-field distribution (Fig. 6). This is also in line with the expectations since the void are not much smaller than the operating wavelength as it is required by the Maxwell-Garnett model.

III. ENCODING STRATEGY

The preceding section highlights the potential for increased resonance and antiresonance diversities by incorporating various void configurations within the 3D chipless tag. By leveraging the number and specific values of these resonances, a unique identification code can be established.

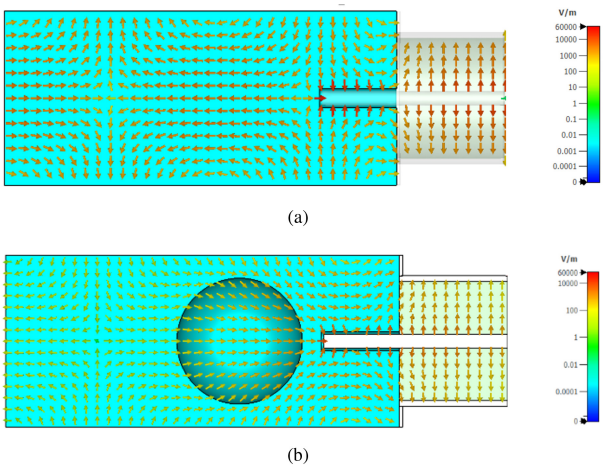

FIGURE 6. Electric field plots of (a) SI equivalent with effective ϵ_r, calculated by Maxwell Garnett, and (b) Actual structure with the circular void, both at 5.4 GHz.

This encoding approach offers a significant improvement over existing solutions, not only in terms of potential encoded bit capacity but also in the associated tag size, which can be considerably reduced. While the dataset containing the resonator's Zero-Crossing Points (ZCPs) presents a viable option for encoding, such a scheme, to be effective for anti-counterfeiting purposes, must guarantee the following key characteristics:

- a unique and uncloneable signature associated with each tag.
- temporal stability of the signature (response that does not change with time).
- efficient retrieval of the tag's electromagnetic signature [4].

A. DESIGN WORKFLOW

As illustrated pictorially in Fig. 4, the variations of the four distinct configurations generate a unique and individual dataset of the imaginary part of the input impedance $Im(Z_{in})$. This dataset encompasses a specific number of resonances and antiresonances (N_{freso}), represented in the form of zero-crossing points (ZCPs). These ZCPs serve as identifiers, effectively characterizing the unique properties of each tag. Subsequently, the Euclidean distances between the ZCPs of each dataset is calculated as:

$$d_{a-b} = \sqrt{\sum_{x=1}^{N_{freso}} (f_{xa} - f_{xb})^2} \tag{3}$$

where, f_{xa} and f_{xb} are the xth order resonance/antiresonance for the individual datasets a and b. It is worth noting here that the $Im(Z_{in})$ crosses zero more than once within the frequency band of interest, and the Euclidean distance computes this difference in the individual ZCPs of the dataset. Within the context of fabrication and measurement accuracy, a tolerance radius (r_{tol}) is established. This parameter serves as a quantitative measure of allowable deviations during the fabrication and measurement inaccuracies of the tags. When analyzing the Zero-Crossing Point (ZCP) response of these tags, it is observed that some tag responses overlap. This overlap signifies redundancy within the dataset, as these overlapping tags essentially provide the same information. To address this redundancy and optimize the dataset for efficiency, a systematic approach to tag elimination is implemented. This optimization process prioritizes minimizing the number of tags removed while simultaneously eliminating all instances of overlap. Furthermore, the dataset is progressively updated with each iteration, ensuring that the elimination process remains effective throughout the analysis. Fig. 7 visually depicts the workflow employed for optimizing the dataset. Each dataset undergoes segregation and receives a unique identifier based on its specific parameter (location and size of the air-voids) values. This segregation facilitates the targeted application of the aforementioned optimization process. The resulting optimized dataset provides a valuable metric: the maximum achievable number of independent tags under the given constraints of N_{freso} and r_{tol}. Independent tags, in this context, refer to tags with distinct ZCP responses, offering non-redundant information. Finally, the tag utilization percentage is calculated. This percentage reflects the proportion of independent tags relative to the total number of tags within the dataset for each considered r_{tol} value.

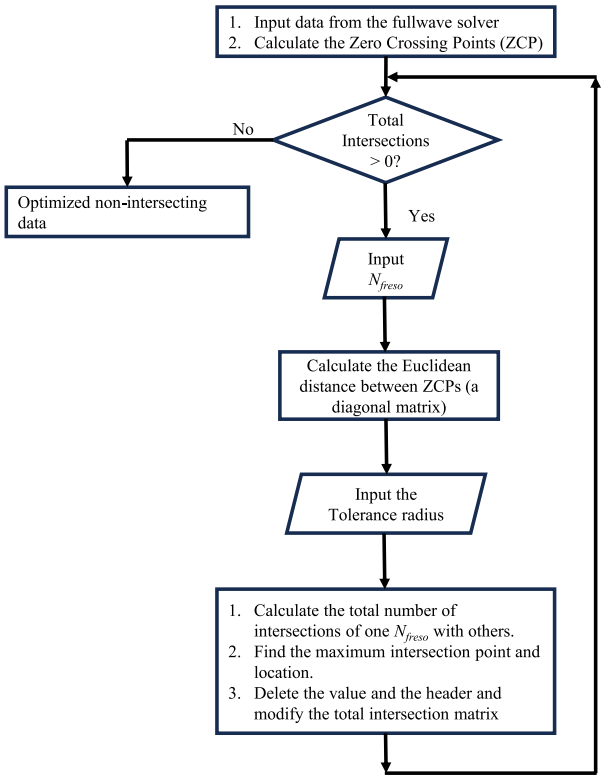

FIGURE 7. Design workflow for retrieval of unique tags.

B. TOLERANCE ANALYSIS

A key aspect of this research involves a tolerance analysis that investigates the relationship between the number of

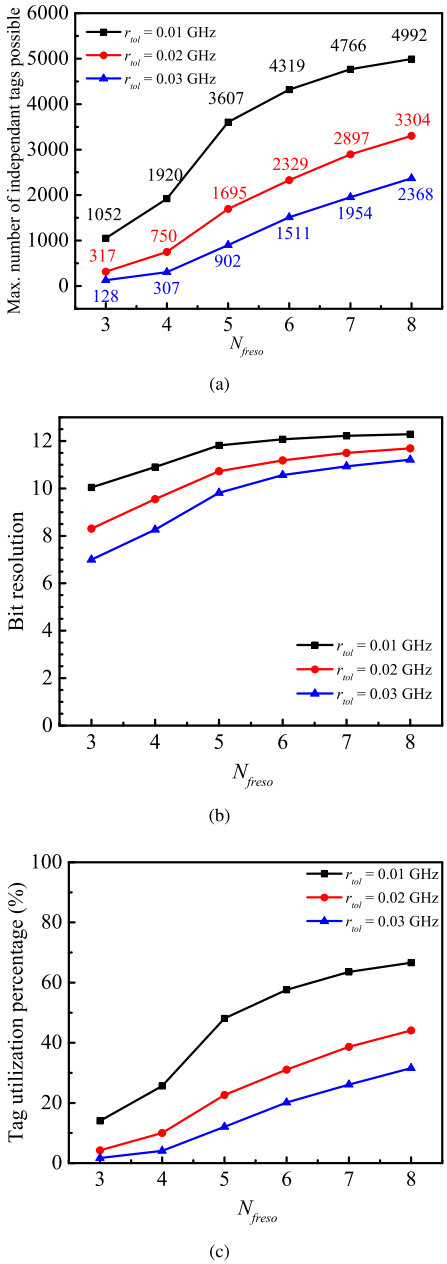

FIGURE 8. (a) Maximum number of independent tags possible, (b) Bit resolution, and (c) Tag utilization percentage, with variation in N_{freso} for different datasets of r_{tol}.

independent tags and the tolerance radius (r_{tol}). This analysis essentially explores how the precision of fabrication and measurement, captured by r_{tol}, influences the feasibility of creating unique tags. The tolerance radius has been systematically varied across a range of values, from 0.01 GHz to 0.03 GHz in increments of 0.01 GHz, with variation of N_{freso} from 3 to 8 in increments of 1. This analysis considers a dataset of approximately 8,000 simulated tags, providing valuable insights visualized in Fig. 8(a).

Transforming the number of tags to the bit resolution results in Fig. 8(b), with 2^x denoting the number of independent tags possible. The analysis reveals an interesting trend:

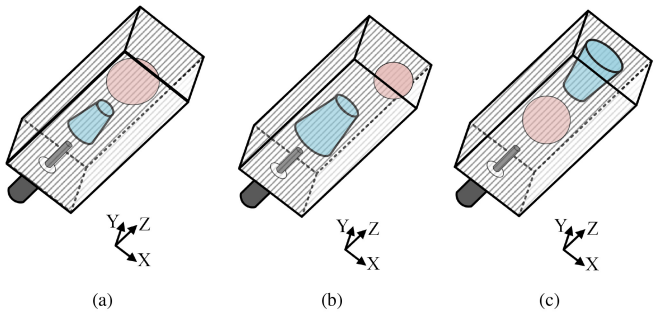

FIGURE 9. Three particular test tags (a) #1, (b) #2, and (c) #3.

the rate of increase in the number of tags is significantly higher for lower N_{freso} values. This trend diminishes at higher N_{freso} values. This observation can be attributed to two factors:

- the limitations of the dataset size, and
- the inclusion of a larger number of tags within the lower N_{freso} range.

Our analysis approach adopts a minimum N_{freso} value of 3, corresponding to three ZCPs in the frequency band of interest. The corresponding number of tags at this N_{freso} level serves as the initial value for subsequent analysis, ensuring a consistent reference point.

Fig. 8(c) discusses on the tag utilization percentage, indicating the proportion of total tags that can be effectively utilized within the entire set of tags simulated. The analysis reveals that approximately 66% of the total tags can be utilized effectively with a tolerance radius of 0.01 GHz.

C. TEST CASE-SIMULATION STUDY

To have a better understanding of the design workflow, three tags have been chosen as shown in Fig. 9, marked #1 - #3. These tags have been analyzed for the frequency band from 4.1 - 4.4 GHz for the ease of understandability of its operation. The *Im* (Z_{in}) have been computed for all the three test tags, from which the ZCP has been evaluated. The Euclidean distance can be calculated using eqn. (3) as: $d_{2\text{-}1} = 0.007$, $d_{3\text{-}1} = 0.077$, and $d_{3\text{-}2} = 0.07$. Now, with a tolerance radius r_{tol} of 0.02 GHz, the $d_{2\text{-}1}$ value overlap, as shown in Fig. 10. Hence, following workflow of Fig. 7, one of the tags #1 or #2 needs to be eliminated. On the contrary, $d_{3\text{-}1}$ and $d_{3\text{-}2}$ fall outside the r_{tol} and hence forms a non-overlapping set. Thus, from the set of three tags, two tags (#3 and either #2 or #1) form a non-overlapping and unique subset.

IV. PROTOTYPES, MEASUREMENTS AND INTEGRATION

A. TESTING - PREPERM

A set of tags have been fabricated with PREPERM ®ABS1000 ($\epsilon_r = 10$, $\tan\delta = 0.003$) and tested to validate the conjecture with a $= b = 15$ mm, and $d = 34.5$ mm. The fabrication comprises broadly of the following stages:

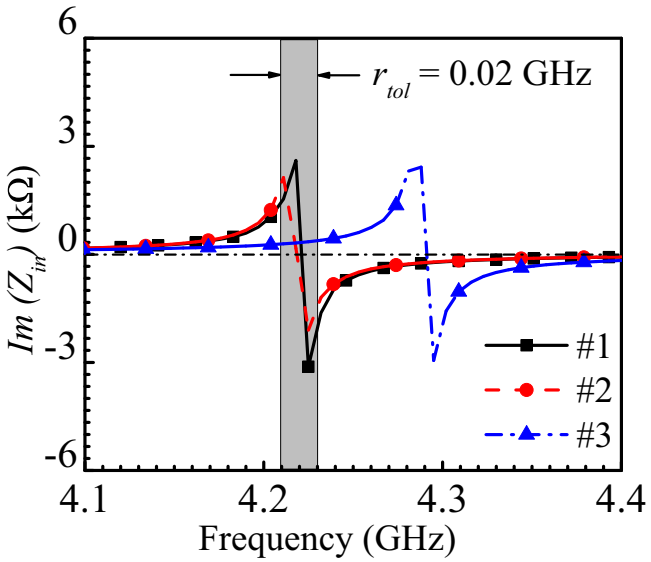

FIGURE 10. Imaginary (Z_{in}) vs. frequency for the three test tags with r_{tol} of 0.02 GHz.

- 3D print with the substrate, which have been done using Fused Deposition Modeling technique on Anycubic I3 Mega [34] using a layer resolution of 0.2 mm;
- Spray a layer of copper conducting paint and immerse in activator;
- Electroplate a thicker layer ($\sim$ 0.1 mm) of copper.

The fabrication workflow is schematically shown in Fig. 11. Additionally, to cross verify and validate the effect of copper deposition in electroplating, a similar set of tags have been copper-taped and the results have been compared. One particular test tag which has been copper taped has been shown along with the copper sprayed counterparts in Fig. 12 for reference. Both the copper sprayed and the taped versions show similar responses and hence their results have not been shown separately for the brevity of the paper. The measured resonator characteristics, for a particular test tag, in terms of the S_{11}-parameter, the real and the imaginary components of the input impedances, ($Re(Z_{in})$) and ($Im(Z_{in})$), respectively, have been shown through Fig. 13, confirming their close agreement with the simulated results, especially at lower operating frequencies. The measured responses have some discrepancies which can be attributed to the fabrication procedure, and tolerances of the 3D printer.

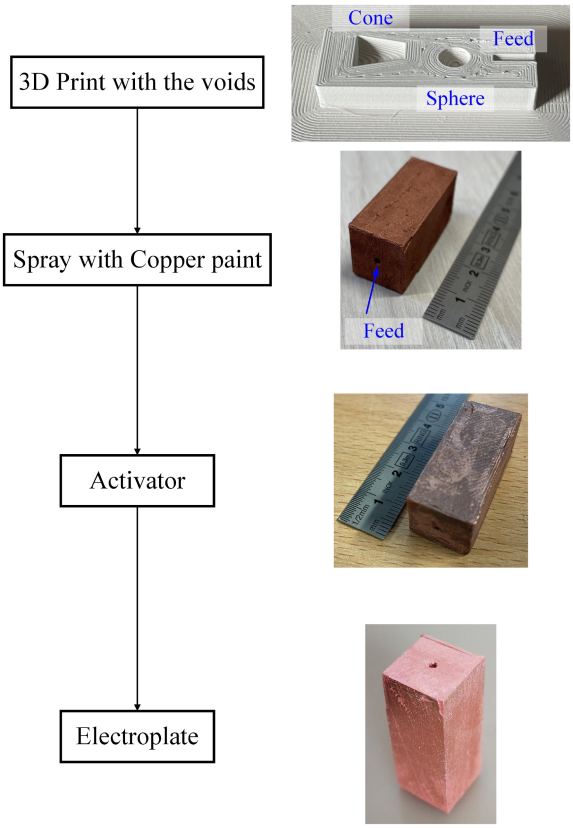

FIGURE 11. Fabrication workflow.

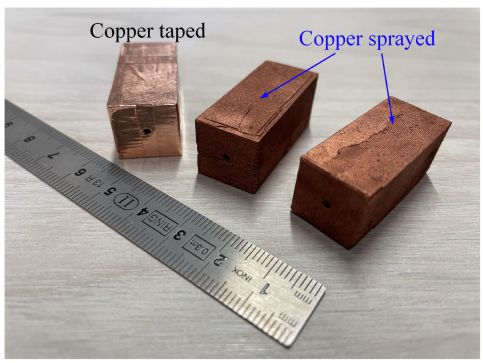

FIGURE 12. Tag with copper taped and sprayed counterparts.

B. PLA – A LOW-COST ALTERNATIVE

As stated before, the analysis till now has been performed on PREPERM® ABS1000 having $\epsilon_r = 10$, tan $\delta = 0.003$. Although, such a substrate is the preferred choice given its low loss tangent and the high permittivity; the spool procurement cost is relatively high. Moreover, loss tangent effects only the Q-factor, rather than affecting its resonant frequencies [35]. Subsequently, the designs have been tried with low-cost PLA, with $\epsilon_r = 2.62$ and tan $\delta = 0.05$ at 2.4 GHz. A similar encoding strategy, as discussed in the previous section for PREPERM®ABS1000 has been performed, the results being shown in Fig. 14, with the same number of datasets being analyzed and subsequently optimized. As is well evident, one has lesser number of independent tags with PLA as compared to PREPERM, which is because of its lower/ inferior material characteristics, but as one moves towards analyzing higher N_{freso}, the bit resolution, although less in PLA, reaches near that of the PREPERM. Hence, it can be inferred that with a lower overall fabrication cost, one can attain a *near-similar* bit resolution, as that obtained with the PREPERM. The PLA tags having the same dimensions as the PREPERM ones have been fabricated and measured to corroborate the results, and they are found to be in good agreement, as portrayed

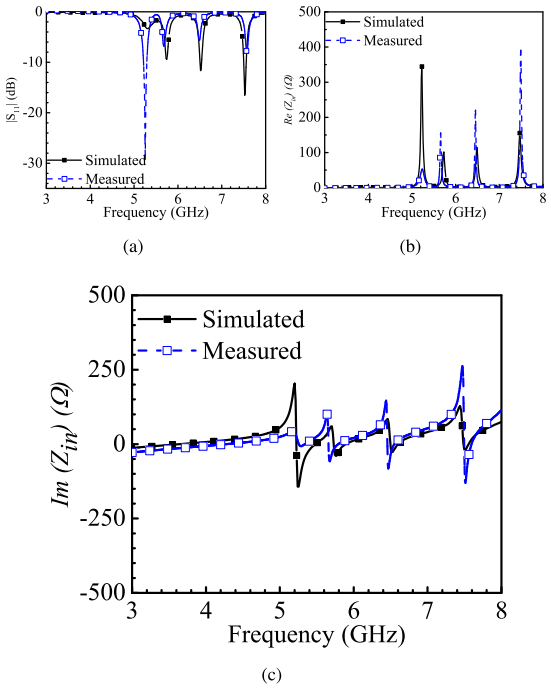

FIGURE 13. Simulated and measured characteristics for a particular test tag: (a) S_{11} parameter, (b) *Re* (Z_{in}), and (c) *Im* (Z_{in}).

TABLE 2. Antiresonances and resonances: PLA.

Antiresonances (GHz)		Resonances (GHz)	
Simu.	Meas.	Simu.	Meas.
7.98	8.0	8.47	8.5
9.77	9.8	10.14	10.1
10.54	10.6	11.76	11.7
11.83	11.9	13.58	13.5
13.7	13.7	14.72	14.7

through the resonances and antiresonances in Table 2. An upshift in operating frequency can be observed which is due to the lower ϵ_r of PLA as compared to PREPERM [35]. A cost analysis has also been performed for two identical tag designs, with PLA, weighing 8 g; and PREPERM, weighing 10 g. The tag fabrication cost with PLA is around 0.16 £, which is roughly 2 £ for PREPERM. This comes at a cost of downshifting the resonance/ antiresonance frequencies, and is up to the end-user to choose, based on his/her reader specifications. The PREPERM having a higher ϵ_r than the PLA results in lowering of the resonances/antiresonances, which is beneficial since the PREPERM based tag can be read with affordable hardware, thus lowering the overall system cost.

C. INTEGRATION IN A SYSTEM

An envisioned practical application of the tag is its integration within a system. This tag should act as an additional security layer in the blockchain management making it ideal for logistics, inventory management, and asset tracking.

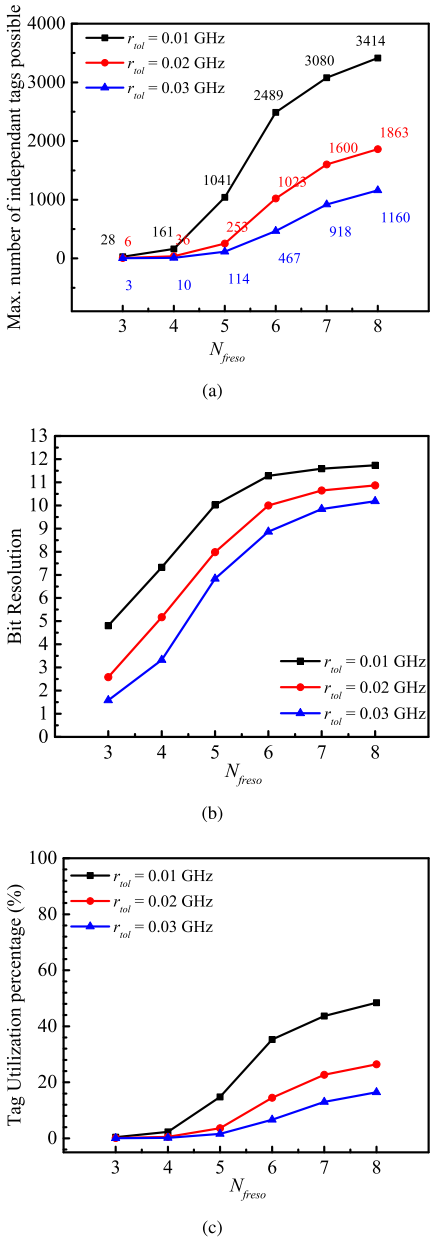

FIGURE 14. (a) Maximum number of independent tags possible, (b) Bit resolution, and (c) Tag utilization percentage, with variation in N_{freso} for different datasets of r_{tol}, all for PLA.

Such a tag would be physically attached to the product, the reader unit would comprise of a portable network analyzer and a probe with SMA connector. The tag would be probed physically (plug-and-play), and its response would be recorded and validated, the schematic being shown in Fig. 15(a). Based on the operating frequencies of the tag, either a handheld-VNA, or nanoVNA can be used as a reader. The coaxial cable (shown in blue) connects the tag to the reader, which extracts the data file for further processing and confirmation of the product authenticity. As an example, the tag has been incorporated inside a test item (a leather bag) (see Fig. 15(b)) and measured. Since the tag

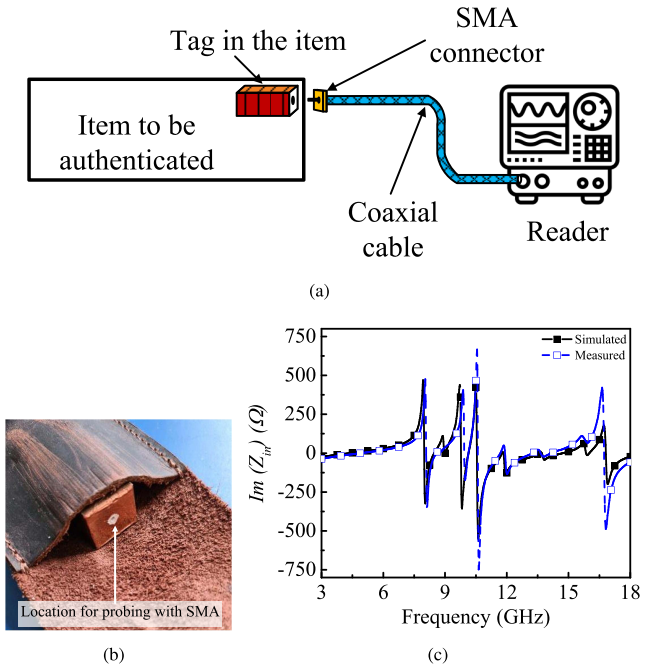

FIGURE 15. (a) Schematic of the test setup, (b) Actual tag incorporated within a leather bag (item), and (c) Simulated and measured responses ($Im\ (Z_{in})$) of the system.

structure is fully metallized, it is expected that it confines the electromagnetic fields within its geometry and hence maintain its impedance characteristics with incorporation in the system. This is confirmed from the standalone simulated and system incorporated measured responses, portrayed in Fig. 15(c), with minor shifts which can majorly be attributed to the fabrication inaccuracy, but within the limits and tolerable error percentages. Hence, such an incorporation within the system holds a potential to enhance the sensitivity and design more efficient and resilient chipless tags [36].

V. CONCLUSION

In this work, an innovative Chipless 3D-printed tag with high encoding scheme has been investigated. Air voids have been created inside the solid infill structure and has been strategically varied to increase the number of encoding states, hence obtaining a larger tag utilization efficiency. A robust optimization scheme calculates the zero crossing points and eliminates the overlapping tags, resulting in unique tags which can act as identifiers for efficient detection of a genuine product from its look-alike fake counterpart, taking into account the tolerant radii of the fabrication system. Two sets of dielectrics (PREPERM®ABS1000 and PLA) have been used to validate the proposed approach. Measurements corroborate the simulated data. Subsequently, one test tag has been incorporated inside a system to validate its operability. Such a plug-and-play tag can form a very robust system, adding another layer of security to the blockchain management, making it suitable for anti-counterfeiting applications.

ACKNOWLEDGMENT

The authors would like to thank Ing. Franchina for helping in the fabrication and measurement of the prototypes.

REFERENCES

[1] A. Nill and C. J. Shultz II, "The scourge of global counterfeiting," *Bus. Horizons*, vol. 39, no. 6, pp. 37–43, 1996.
[2] A. K. Deisingh, "Pharmaceutical counterfeiting," *Analyst*, vol. 130, no. 3, pp. 271–279, 2005.
[3] M. G. Harvey, "Industrial product counterfeiting: Problems and proposed solutions," *J. Bus. Ind. Market.*, vol. 2, no. 4, pp. 5–13, 1987.
[4] B. Danev, D. Zanetti, and S. Capkun, "On physical-layer identification of wireless devices," *ACM Comput. Surv.*, vol. 45, no. 1, pp. 1–29, 2012.
[5] Y. Li, X. Chen, Y. Lin, G. Srivastava, and S. Liu, "Wireless transmitter identification based on device imperfections," *IEEE Access*, vol. 8, pp. 59305–59314, 2020.
[6] P. Tuyls and L. Batina, "RFID-tags for anti-counterfeiting," in *Proc. Cryptogr. Track RSA Conf.*, 2006, pp. 115–131.
[7] L. Peng, J. Zhang, M. Liu, and A. Hu, "Deep learning based RF fingerprint identification using differential constellation trace figure," *IEEE Trans. Veh. Technol.*, vol. 69, no. 1, pp. 1091–1095, Jan. 2020.
[8] J. Zhang, R. Woods, M. Sandell, M. Valkama, A. Marshall, and J. Cavallaro, "Radio frequency fingerprint identification for narrow-band systems, modelling and classification," *IEEE Trans. Inf. Forensics Security*, vol. 16, pp. 3974–3987, 2021.
[9] G. Ruffato, R. Rossi, M. Massari, E. Mafakheri, P. Capaldo, and F. Romanato, "Design, fabrication and characterization of computer generated holograms for anti-counterfeiting applications using OAM beams as light decoders," *Sci. Rep.*, vol. 7, no. 1, 2017, Art. no. 18011.
[10] J. Miao, X. Ding, S. Zhou, and C. Gui, "Fabrication of dynamic holograms on polymer surface by direct laser writing for high-security anti-counterfeit applications," *IEEE Access*, vol. 7, pp. 142926–142933, 2019.
[11] T. Wu, J. Ma, P. Su, H. Kao, and Y. Cui, "Three-dimensional anti-counterfeiting method based on reflective volume holography," in *Proc. 10th SPIE Holography, Diffractive Opt., Appl.*, 2020, pp. 137–142.
[12] T. Uematsu, "Combining overt and covert anti-counterfeiting technologies for securities," in *Proc. Opt. 6th SPIE, Secur. Count. Deterrence Techn.*, 2006, pp. 248–255.
[13] S. Tedjini et al., "Hold the chips: Chipless technology, an alternative technique for RFID," *IEEE Microw. Mag.*, vol. 14, no. 5, pp. 56–65, Jul./Aug. 2013.
[14] F. Costa, S. Genovesi, and A. Monorchio, "A chipless RFID based on multiresonant high-impedance surfaces," *IEEE Trans. Microw. Theory Techn.*, vol. 61, no. 1, pp. 146–153, Jan. 2013.
[15] A. Vena, E. Perret, and S. Tedjini, "Chipless RFID tag using hybrid coding technique," *IEEE Trans. Microw. Theory Tech.*, vol. 59, no. 12, pp. 3356–3364, Dec. 2011.
[16] F. Costa, S. Genovesi, A. Monorchio, and G. Manara, "A robust differential-amplitude codification for chipless RFID," *IEEE Microw. Wireless Compon. Lett.*, vol. 25, no. 12, pp. 832–834, Dec. 2015.
[17] M. Omer and G. Y. Tian, "Indoor distance estimation for passive UHF RFID tag based on RSSI and RCS," *Measurement*, vol. 127, pp. 425–430, Oct. 2018.
[18] S. Preradovic and N. C. Karmakar, "Chipless RFID: Bar code of the future," *IEEE Microw. Mag.*, vol. 11, no. 7, pp. 87–97, Dec. 2010.
[19] I. Balbin and N. C. Karmakar, "Phase-encoded chipless RFID transponder for large-scale low-cost applications," *IEEE Microw. wireless Compon. Lett.*, vol. 19, no. 8, pp. 509–511, Aug. 2009.
[20] S. Genovesi, F. Costa, A. Monorchio, and G. Manara, "Chipless RFID tag exploiting multifrequency delta-phase quantization encoding," *IEEE Antennas Wireless Propag. Lett.*, vol. 15, pp. 738–741, 2015.
[21] M. A. Kossel, R. Kung, H. Benedickter, and W. Biichtokd, "An active tagging system using circular-polarization modulation," *IEEE Trans. Microw. Theory Tech.*, vol. 47, no. 12, pp. 2242–2248, Dec. 1999.
[22] S. Genovesi, F. Costa, F. A. Dicandia, M. Borgese, and G. Manara, "Orientation-insensitive and normalization-free reading chipless RFID system based on circular polarization interrogation," *IEEE Trans. Antennas Propag.*, vol. 68, no. 3, pp. 2370–2378, Mar. 2020.

[23] C. Herrojo et al., "Time-domain-signature chipless RFID tags: Near-field chipless-RFID systems with high data capacity," *IEEE Microw. Mag.*, vol. 20, no. 12, pp. 87–101, Dec. 2019.
[24] K. R. Brinker and R. Zoughi, "A review of chipless RFID measurement methods, response detection approaches, and decoding techniques," *IEEE Open J. Instrum. Meas.*, vol. 1, pp. 1–31, Aug. 2022, doi: 10.1109/OJIM.2022.3196746.
[25] Z. Ali et al., "Authentication using metallic inkjet-printed chipless RFID tags," *IEEE Trans. Antennas Propag.*, vol. 68, no. 5, pp. 4137–4142, May 2020.
[26] R. de Amorim, R. Siragusa, N. Barbot, G. Fontgalland, and E. Perret, "Millimeter wave chipless RFID authentication based on spatial diversity and 2-D classification approach," *IEEE Trans. Antennas Propag.*, vol. 69, no. 9, pp. 5913–5923, Sep. 2021.
[27] S. Terranova, F. Costa, G. Manara, and S. Genovesi, "Three-dimensional chipless RFID tags: Fabrication through additive manufacturing," *Sensors*, vol. 20, no. 17, p. 4740, 2020.
[28] S. Mondal, K. P. Wijewardena, S. Karuppuswami, N. Kriti, D. Kumar, and P. Chahal, "Blockchain inspired RFID-based information architecture for food supply chain," *IEEE Internet Things J.*, vol. 6, no. 3, pp. 5803–5813, Jun. 2019.
[29] K. J. Bois, L. F. Handjojo, A. D. Benally, K. Mubarak, and R. Zoughi, "Dielectric plug-loaded two-port transmission line measurement technique for dielectric property characterization of granular and liquid materials," *IEEE Trans. Instrum. Meas.*, vol. 48, no. 6, pp. 1141–1148, Dec. 1999.
[30] A. K. Jha and M. J. Akhtar, "A generalized rectangular cavity approach for determination of complex permittivity of materials," *IEEE Trans. Instrum. Meas.*, vol. 63, no. 11, pp. 2632–2641, Nov. 2014.
[31] C. A. Balanis, *Antenna Theory: Analysis and Design*. Hoboken, NJ, USA: Wiley, 2016.
[32] J. M. Garnett, "Colours in metal glasses, in metallic films, and in metallic solutions. II," *Philosoph. Trans. Roy. Soc. London Ser. A*, vol. 205, pp. 237–288, Jan. 1906.
[33] J. C. M. Garnett, "Colours in metal glasses and in metallic films," *Proc. Royal Soc. London*, vol. 73, nos. 488–496, pp. 443–445, 1904. [Online]. Available: http://doi.org/10.1098/rspl.1904.0058
[34] "Anycubic I3 mega." Accessed: Sep. 2023. [Online]. Available: https://anycubic.it/products/anycubic-i3-mega
[35] K. R. Brinker and R. Zoughi, "Tunable chipless RFID pressure sensor Utilizing additive manufacturing—Model, simulation, and measurement," *IEEE Trans. Instrum. Meas.*, vol. 72, pp. 1–13, Jan. 2023.
[36] D. P. Mishra and S. K. Behera, "Resonator based chipless RFID: A frequency domain comprehensive review," *IEEE Trans. Instrum. Meas.*, vol. 72, pp. 1–16, 2023, doi: 10.1109/TIM.2022.3225027.

SUVADEEP CHOUDHURY (Senior Member, IEEE) received the M.Tech. degree from The University of Burdwan and the Ph.D. degree from the Department of Electronics and Electrical Communication Engineering, Indian Institute of Technology (IIT) Kharagpur, India, in 2019.

He worked as a Technical Lead with the Research and Development Wing, HCL Tech. Pvt. Ltd. from 2019 to 2020, and briefly as a Postdoctoral Research Associate with IIT Kharagpur. He jointly with Space Application Center, ISRO from 2020 to 2021. He joining The LNM Institute of Information Technology, Jaipur, India, as an Assistant Professor in 2021. He is currently a Postdoctoral Researcher with the Dipartimento di Ingegneria dell'Informazione, University of Pisa, Pisa, since 2023, on-leave from The LNMIIT Jaipur. He expertise in the design and development of low profile, high gain antennas, SIW based antennas, RFID tags, and wearable antennas. He has authored 1 book, 3 patents (granted), published several journals and conferences of repute and serves as an active reviewer of multiple prestigious IEEE TRANSACTIONS AND LETTERS. He is the recipient of the Prestigious IEEE APS-Fellowship from 2024 to 2025. He was awarded the University Gold medal in 2013. He is currently a Senior Member of URSI, and a Life Member of IETE.

FILIPPO COSTA (Senior Member, IEEE) received the M.Sc. degree in telecommunication engineering and the Ph.D. degree in applied electromagnetism from the University of Pisa, Pisa, Italy, in 2006 and 2010, respectively.

In 2009, he was a Visiting Researcher with the Department of Radio Science and Engineering, Aalto University, Espoo, Finland. From 2015 to 2017, he was a Short-Term Visiting Researcher with the Grenoble Institute of Technology, Valance, France, and the University Rovira I Virgili, Tarragona, Spain. He is currently an Associate Professor with the Dipartimento di Ingegneria dell'Informazione, University of Pisa. His current research interests include metamaterials, metasurfaces, antennas, and radio frequency identification. He was a recipient of the Young Scientist Award of the URSI International Symposium on Electromagnetic Theory in 2013, the URSI General Assembly in 2014, and the URSI AT-RASC in 2015. He serves as an Associate Editor for the IEEE TRANSACTIONS ON ANTENNAS AND PROPAGATION, IEEE ANTENNAS AND WIRELESS PROPAGATION LETTERS, IEEE SENSORS LETTERS, *Scientific Reports*, and *Sensors and Electronics*.

GIULIANO MANARA (Life Fellow, IEEE) is currently a Professor with the Dipartimento di Ingegneria dell'Informazione, University of Pisa, Pisa, Italy. Since 1980, he has been collaborating with the Department of Electrical Engineering, Ohio State University, Columbus, OH, USA, where, he was involved in research with ElectroScience Laboratory, Columbus, in 1987. His contributions to the uniform geometrical theory of diffraction and its applications. His research interests include mainly the asymptotic solution of radiation and scattering problems to improve and extend the uniform geometrical theory of diffraction. He has also been engaged in research on numerical, analytical, and hybrid techniques (frequency and time domains), scattering from rough surfaces, frequency selective surfaces, and electromagnetic compatibility. More recently, his research has also been focused on the design of microwave antennas with application to broadband wireless networks, on the development and testing of new microwave materials (metamaterials), and on the analysis of antennas and propagation problems for radio frequency identification systems.

Prof. Manara was elected the Vice-Chair of the International Commission B "Fields and Waves" of URSI (International Radio Science Union) in August 2008. He served as the International Chair for URSI Commission B for the triennium from 2011 to 2014. He has been elected a URSI Fellow in 2017. Since 2021, he has been serving as the Vice-President for URSI.

SIMONE GENOVESI (Senior Member, IEEE) received the Laurea degree in telecommunication engineering and the Ph.D. degree in information engineering from the University of Pisa, Pisa, Italy, in 2003 and 2007, respectively.

From 2004 to 2006, he was a Research Associate with the ISTI Institute of the National Research Council of Italy, Pisa. From 2015 to 2017, he was several times a Short-Term Visiting Researcher with the Grenoble Institute of Technology, Valence, France, and also with University Rovira I Virgili, Tarragona, Spain. Since 2003, he has been collaborating with the Electromagnetic Communication Laboratory, Pennsylvania State University, University Park, PA, USA. He is currently an Associate Professor with the Dipartimento di Ingegneria dell'Informazione, University of Pisa. He is the Coordinator of the Additive Manufacturing founded in the framework of the Departments of Excellence funded by the Italian Ministry of Education, University, and Research. His current research interests include additive manufacturing, sensors, radio frequency identification systems, and reconfigurable antennas. He is an Associate Editor of the IEEE TRANSACTIONS ON ANTENNAS AND PROPAGATION.

Open Access funding provided by 'Università di Pisa' within the CRUI CARE Agreement